Journal of Materials Chemistry C

Bonding similarities and differences between Y–Sb–Te and Sc–Sb–Te phase-change memory materials

Journal:	*Journal of Materials Chemistry C*
Manuscript ID	TC-ART-01-2020-000096.R1
Article Type:	Paper
Date Submitted by the Author:	01-Feb-2020
Complete List of Authors:	Zhou, Yuxing; Xi'an Jiaotong University, School of Materials Science and Engineering Sun, Liang; Xi'an Shiyou University, Key Laboratory of Materials Processing Engineering, College of Materials Science and Engineering Zewdie, Getasew; Xi'an Jiaotong University, School of Materials Science and Engineering Mazzarello, Ricardo; Rheinisch Westfalische Technische Hochschule Aachen Fakultat fur Mathematik Informatik und Naturwissenschaften, Deringer, Volker; University of Oxford, Department of Chemistry Ma, Evan; Johns Hopkins University, Department of Materials Science and Engineering Zhang, Wei; Xi'an Jiaotong University, Materials Science and Engineering

Bonding similarities and differences between Y–Sb–Te and Sc–Sb–Te phase-change memory materials

Yuxing Zhou[1], Liang Sun[2], Getasew M. Zewdie[1], Riccardo Mazzarello[3], Volker L. Deringer[4], Evan Ma[5], Wei Zhang[1,6]*

[1]Center for Advancing Materials Performance from the Nanoscale, State Key Laboratory for Mechanical Behavior of Materials, Xi'an Jiaotong University, Xi'an 710049, China.
[2]Key Laboratory of Materials Processing Engineering, College of Materials Science and Engineering, Xi'an Shiyou University, Xi'an 710065, China
[3]Institute for Theoretical Solid-State Physics, JARA-FIT and JARA-HPC, RWTH Aachen University, Aachen 52056, Germany
[4]Department of Chemistry, Inorganic Chemistry Laboratory, University of Oxford, Oxford OX1 3QR, UK
[5]Department of Materials Science and Engineering, Johns Hopkins University, USA
[6]Xi'an Jiaotong University Suzhou Institute, Suzhou 215123, China

*Email: wzhang0@mail.xjtu.edu.cn

Abstract

The scandium (Sc) - alloyed Sb_2Te_3 phase-change alloy has recently been found to enable ultrafast crystal nucleation due to the formation of Sc-stabilized octahedral motifs in the amorphous phase, rendering cache-type phase-change memory feasible. When yttrium (Y) is added, however, non-octahedral bonding patterns form in the amorphous Sb_2Te_3-based network even though Y has a valence electron configuration similar to that of Sc and also forms perfect octahedral bonding environments with tellurium in the YTe crystal. Here we elucidate the origin of this difference between Sc and Y, by carrying out thorough *ab initio* simulations and orbital-based bonding analyses on amorphous Y-Sb-Te and Sc-Sb-Te compounds. We also demonstrate how the smooth overlap of atomic positions (SOAP) similarity kernel can be used to quantify the structural similarity of local motifs in the amorphous phase with respect to various crystalline yttrium and scandium tellurides, both in the nearest-neighbor shell and beyond. We find that the bonding contrast of Y- and Sc-centered structural motifs in amorphous Sb_2Te_3 stems from their parent crystals at high Te concentrations. The larger atomic radius of Y and the weaker charge transfer when bonded with Te is found to allow more Te neighbors and cause a more open bonding environment, leading to higher coordination numbers and non-octahedral environments. We discuss the implications of the different local environments for practical applications in memory devices.

Introduction

Non-volatile memory technologies, including chalcogenide phase-change materials (PCMs),[1, 2] transition metal oxides,[3, 4] two-dimensional materials[5, 6] and others,[7-9] combine the advantage of persistent storage with fast switching speed, and therefore hold great promise to cope with the explosively increasing demand for data storage and processing. Competitive PCM memory products based on the flagship $Ge_2Sb_2Te_5$ (GST) compound have entered the global memory market very recently.[10, 11] PCMs utilize a pronounced contrast in electrical resistance or optical reflectance between amorphous and crystalline states to encode data.[12] The two states can be reversibly switched – referred to as the SET (crystallization) and RESET (amorphization) operations – by using external voltage or laser pulses. The programming speed can be extremely fast, reaching the level of nanoseconds at elevated temperatures; yet, both the amorphous and crystalline states are thermally stable over decades at room temperature, making them suitable for long-term data storage.[12] The programming volume can also be scaled down to the length scale of a few nanometers.[13, 14] Such special combination of materials properties makes PCMs a strong candidate for non-volatile memory. Yet, the device performance remains to be further improved for next-generation memory and computing chips.[15-17]

The performance of PCM devices in terms of switching speed is primarily hindered by the SET (crystallization) process.[18] For all GST devices, the minimum SET time takes more than 10 ns. Although ample crystalline precursors – ABAB squares (A=Ge/Sb, B=Te) – are present in amorphous GST,[19-23] these structural fragments tend to break rapidly at elevated temperatures.[24-28] To bypass the stochastic nucleation stage, a pre-programming scheme that applies a 10-ns low-magnitude pre-pulse was developed,[29-31] reducing the SET time to 0.5 ns.[29] Recently, an intrinsic materials engineering approach was developed to reduce the stochasticity of nucleation.[32] Based on two critical indictors, small lattice mismatch and strong chemical bonds, a careful materials screening was made over dozens of transition metal tellurides. Scandium was determined to be the optimal alloying element to incorporate into Sb_2Te_3, forming a $Sc_{0.2}Sb_{1.8}Te_3$ alloy (referred to as "SST" hereafter).[32] This design was corroborated by an independent high-throughput screening based on *ab initio* simulations.[33] A new PCM device based on SST was demonstrated to enable a 0.7 ns SET operation in the absence of pre-programming, reaching the speed level of cache-type memories.[32] The enhanced crystallization is mainly due to the stabilization of crystalline precursors as preferential nucleation sites, namely, Sc-Te squares and cubes,[32, 34] through the much stronger covalent and electrostatic interactions of Sc-Te bonds as compared to Sb-Te bonds.[35]

The materials screening approach also suggested yttrium (Y) as another potentially suitable alloying element, because YTe also forms a rocksalt-type structure with high cohesive energy[32]. This potential materials choice is of particular interest for industrial development, as Y is much cheaper than Sc. However, simulations revealed that Y atoms tend to form non-octahedral motifs in the amorphous phase, deviating strongly from the desired crystalline precursors.[32] Parallel studies also showed that $Y_xSb_{2-x}Te_3$ ($x \leq 0.33$) phase-change compounds[36, 37] may improve the

amorphous-state stability due to the more complex structural pattern with respect to the base material Sb_2Te_3. Indeed, as compared to Sc, Y is a more effective alloying element to increase the crystallization temperature and data retention temperature of amorphous Sb_2Te_1.[38, 39] These findings suggest that a careful compositional tuning of Y-Sb-Te might render it a potential candidate for embedded memory applications, with good amorphous-state stability yet rapid switching speed. The elusive scientific question begging for an answer is then why the homologous Sc and Y (with a very similar valence electron configuration of $4s^23d^1$ versus $5s^24d^1$ for the free atoms) would lead to very different structural patterns when incorporated into amorphous Sb-Te alloys.

In the present work, we carry out thorough structural and chemical bonding analyses on amorphous $Y_{0.2}Sb_{1.8}Te_3$ (YST) and various crystalline yttrium tellurides. In comparison with $Sc_{0.2}Sb_{1.8}Te_3$ (SST) and Sb_2Te_3, we elucidate the atomic origin of bonding similarities and differences between Y- and Sc- alloyed Sb_2Te_3. Our work aims to provide an atomic-scale understanding of the emerging SST and YST PCM groups. This fundamental knowledge of their structural characteristics will also guide the design of their suitable applications.

Results and discussion

Structural models of amorphous (a-) YST were generated under the melt-quench scheme using DFT-based AIMD simulations. Starting from a 3×3×3 supercell of rocksalt YST, the model was heated up rapidly to 3000 K for randomization over 20 ps, and was then equilibrated at 1000 K over 30 ps. The resultant liquid model was then quenched down to 300 K in 60 ps to obtain the amorphous state. After holding at 300 K over another 30 ps, we collected the data for structural analysis. Five a-YST models with independent thermal history were generated and analyzed to improve the statistics. The optimized edge length of the cubic supercell is 18.75 Å, corresponding to a theoretical density of 0.0273 $Å^{-3}$ (5.61 g cm^{-3}). For comparison, five a-Sb_2Te_3 and a-SST models were calculated under the same melt-quench scheme using the respective theoretical density, viz. 5.65 g cm^{-3} (Ref. [40]) and 5.53 g cm^{-3} (Ref. [35]). All the amorphous models were quenched down to, and further relaxed at, 0 K for the electronic structure calculations and COHP bonding analyses.

The calculated electronic density of states (DOS) suggests a-YST to be a narrow-gap semiconductor (Figure 1a), just like a-SST[35] and a-Sb_2Te_3.[35, 40] The COHP method dissects the computed electronic structure into antibonding (destabilizing) and bonding (stabilizing) orbital pair interactions. Besides the small antibonding region below the Fermi level, the overall –COHP curve shows bonding interaction in the occupied bands, indicating good chemical stability of a-YST (Figure 1b). Such antibonding feature is consistently found in various crystalline and amorphous PCMs. Resolving these –COHP interactions according to specific pairs of atom types reveals that this antibonding interaction is mostly contributed by the Sb-Te and Te-Te bonds, while Y-Te bonds are shown to be stabilizing throughout (Figure 1b). In addition to covalent

interaction, we have also calculated the charge transfer to assess the electrostatic interaction. As shown in Figure 1c, the Löwdin charge of Y atoms is about ~0.46 |e|, larger than that of Sb and Te atoms, suggesting stronger Coulomb interaction in Y-Te than in Sb-Te contacts. All these bonding features of a-YST are qualitatively similar to those a-SST, despite the more ionic character of Sc atoms with much larger Löwdin charges of ~0.80 |e|,[35] indicating a larger electrostatic contribution to the bonding in SST as compared to YST.

Comparing the local structure of a-YST to that of both the base compound a-Sb_2Te_3 and the homologous a-SST (Figure 2), the major difference is found in the bonding angle and local motifs surrounding the transition-metal atoms. The majority of Sb atoms are in defective octahedral configurations in a-Sb_2Te_3, and this remains the same upon Y and Sc alloying. A clear contrast is observed around the Sc and Y atoms, which form octahedral and non-octahedral bonds, respectively, as evidenced by the angular distribution functions (ADF) shown in Figure 2a. The ADFs calculated for Sb and Sc atoms show a major peak around 90^o (corresponding to rocksalt-like motifs), while the distribution of bond angles around Y atoms is more diverse and appears to show a bimodal distribution, with peaks around ~78^o and ~140^o. These non-octahedral Y-centered motifs in a-YST are not a consequence of the very limited Y-Sb bonds (< 2%) that are formed during the rapid quenching process, but are rather due to the heteropolar Y-Te bonds, in stark contrast with the 90° bond angles in crystalline, rocksalt-type YTe.

In addition, Y atoms tend to form longer bonds with Te atoms as compared with Sc and Sb atoms, as shown by the partial pair correlation functions (PCFs) in Figure 2b. In a-Sb_2Te_3, all the three partial PCFs show a major peak at ~2.9 Å, consistent with previous studies.[40-42] In a-YST, the Y-Te bonds show a peak at ~3.3 Å, much longer than the Sb-Te bonds. In a-SST, however, the bond lengths of Sc-Te and Sb-Te bonds are compatible. Also, Sc atoms tend to group together to form Sc-Te squares, which results in a clear peak in the Sc-Sc PCF around 4 Å, corresponding to the Sc-Sc distance diagonally across the Sc-Te squares. Such a trend is consistently observed in all a-SST models, and these desired crystalline precursors of high bond strength give rise to the significantly reduced stochasticity of nucleation in a-SST.[32]

To gain further understanding of the bonding contrast between a-YST and a-SST, we have carried out quantitative structural analyses using the SOAP formalism.[43] SOAP was initially developed for use in machine learning potential fitting[43] but is also a highly useful approach for structural analyses.[44] In particular, SOAP can be used to quantify the similarity of all individual atoms in structural models of amorphous phases to the corresponding crystalline compounds[45, 46] and to generate insightful structural maps of liquid, amorphous, and crystalline phases.[47, 48] As shown in Figure 3, to describe the local environment of a given atom, i, Gaussian functions with broadness σ_{at} are placed on each atomic position in a given sphere with a cutoff of r_c. The local density of atoms, $\rho_i(\boldsymbol{r})$, is then a sum over all of these Gaussian functions within this sphere: $\rho_i(\boldsymbol{r}) =$

$\sum_k \exp\left[-\frac{(\boldsymbol{r}-\boldsymbol{r_{ik}})^2}{2\sigma_{\text{at}}^2}\right]$. The SOAP kernel *k*, for a pair of local environments, is obtained via the overlap of atomic densities of these two local environments, integrated over all three-dimensional rotations θ: $k_{i,j} = \int d\theta |\rho_{\boldsymbol{i}}(\boldsymbol{r})\rho_{\boldsymbol{j}}(\theta\boldsymbol{r})d\boldsymbol{r}|^2$. To efficiently calculate the SOAP kernel, the atomic density is expanded in a basis of radial functions and spherical harmonics: $\rho_i(\boldsymbol{r}) = \sum_{nlm} c_{nlm}^{(i)} R_n(r) Y_{lm}(\boldsymbol{r})$. With the obtained combination coefficients c_{nlm}, the SOAP kernel can then be calculated via a dot product of two atomic density vectors, with *n* and *l* as convergence parameters running up to a suitable maximum (here, we choose $n_{\text{max}} = 14$ and $l_{\text{max}} = 8$). The SOAP vectors are computed using the DScribe package.[49]

In short, the SOAP kernel value, ranging from 0 to 1, characterizes the degree of structural similarity between two given atomic densities. It was recently shown[46] that combining SOAP kernels with various cutoff radii and appropriately adjusted smoothness can be a useful approach for concurrently analyzing short- and longer-range order in amorphous structures. We follow a similar approach here: we define one SOAP kernel which considers only the nearest-neighbor (NN) environment, and one which also takes into consideration the next-nearest-neighbor (NNN) shell. The cut-offs are chosen to be the position of the first and second valleys in the respective PCF (Figure 2b) to include all atoms in the first atomic shell (for NN environment, $\sigma_{\text{at}} = 0.3$ Å) and the second atomic shell (for NNN environment, $\sigma_{\text{at}} = 0.6$ Å).[46]

In Figure 3b, we highlight selected Y-centered structural motifs in a-YST. The remaining bonds are drawn as semi-transparent for better clarity. The SOAP analysis was performed for all local environments of Y atoms in five independent a-YST models, and each of these environments was compared to that of an Y atom in crystalline rocksalt-type YTe [50] (Figure 3c). Both the NN- and the NNN-SOAP values are rather low, indicating a clear mismatch in Y-centered motifs between the a-phase and the c-phase. Given the low Y concentration, the local environment of Y atoms is Te-rich. We carry out similar SOAP analysis for a-YST and Te-rich yttrium telluride crystals. Three crystalline phases have been reported in the literature: orthorhombic Y_2Te_3 (*Fddd*),[51] tetragonal YTe_2 (*P*4/*nmm*),[52] and orthorhombic YTe_3 (*Cmcm*),[53] as depicted in Figure 3 d-f. In Y_2Te_3, the Y atoms are still octahedrally coordinated, while the bonding situation gets more complex in YTe_2 and YTe_3, as the Y atoms form 9 short bonds of 3.1-3.3 Å with Te atoms, and the bond angles are no longer close to 90°. The (dis)similarity in octahedral and non-octahedral bonding configurations of different yttrium telluride crystals is quantified by the SOAP analysis and is presented in Table 1. For the non-octahedral case, YTe_2 and YTe_3 share the same basic structural fragment, but differ in the second nearest neighbor in that a visible van der Waals gap is present in the latter phase. It is noted that the bond angles in crystalline YTe_2 and YTe_3, such as 75° and 138°, correspond to the ADF peaks in a-YST (Figure 2a), and the SOAP analysis quantifies this behavior, as the SOAP similarity of a-YST is increased when compared to crystalline YTe_2 and YTe_3.

Therefore, the complex structural pattern around Y atoms in the a-YST is more like that of yttrium telluride crystals with high Te concentration, arising from the same bonding character prevalent in the latter cases.

We performed similar analysis on a-SST over various crystalline scandium tellurides (Figure 4). We focus, again, on those crystalline compounds exhibiting high Te concentrations, i.e. hexagonal ScTe ($P6_3/mmc$),[54] and Sc_2Te_3 with its three crystalline polymorphs – rhombohedral, cubic, and orthorhombic –, as discussed in our previous work.[35] Scandium telluride crystals with even higher Te concentration have not been reported to our knowledge. All four crystalline scandium telluride structures are shown in Figure 4, together with an a-SST model. In all four crystalline structures, Sc atoms are in a perfect octahedral coordination. Only a fraction of Te atoms form non-octahedral bonds with Sc atoms in ScTe and rhombohedral Sc_2Te_3. The SOAP analysis, in particular the NN-SOAP values, shows a high value around 0.8 for Sc-centered motifs in a-SST with respect to the four crystalline phases. The only difference is that not all Sc atoms have six Te neighbors in the amorphous phase.

The SOAP analysis reveals that both Y- and Sc-centered structural motifs in the amorphous phases closely resemble their respective crystalline counterparts. The relatively large values of nearest-neighbor similarities around Sc atoms in a-SST and in all four crystalline scandium tellurides point toward a similar, rock-salt-like, local bonding configuration. This is in stark contrast with the yttrium case. Despite the very similar valence shell configuration, the two homologous elements have very different coordination environments in the Te-rich case that we study here. We attribute this structural and bonding contrast to the difference in atomic radii and in the degree of charge transfer of Sc and Y atoms when bonded with Te atoms. The larger atomic radius of Y, due to the additional electron shell, leads to the formation of longer bonds with Te, presumably allowing for larger structural diversity in the environment. Due to the smaller charge transfer between Y and Te atoms, the energy penalty of Te-Te bonds inside the Y bonding environment is smaller, allowing the presence of more than six Te neighbors forming non-octahedral bonds (Figure 3). This explains why Y atoms have 9 Te neighbors in YTe_2 and YTe_3 crystals, and more than 7 Te neighbors in a-YST (using a Y-Te bond distance cutoff of 3.4 Å). In the Sc case, the smaller Sc-Te bonds and the larger negative charges of Te atoms[35] tend to maximize the Te-Te distances in the Sc-centered environment to reduce the energy penalty, forming nearly perfect octahedra (Figure 4).

Given the high chemical strength of Sc-centered crystalline precursors in a-SST, the stochasticity of crystal nucleation is sharply reduced, leading to more than one order of magnitude faster SET speed in the SST-based memory devices than in the GST-based ones.[32] However, the desired crystalline precursors could also increase the nucleation rate of a-SST at room temperature, thus potentially weakening the thermal stability of a-SST. Nevertheless, both the crystallization temperature (150 ^{o}C) and the 10-year data retention at temperature 87 ^{o}C of a-SST were shown to be comparable to those of a-GST.[32] It was recently understood that the presence of Sc also

increases the viscosity of the system, rendering SST liquid dynamics exceedingly sluggish upon cooling.[55] Thus, the barrier for crystal growth is markedly increased near room temperature. In YST, the Y-Te bonds are also of high chemical strength, which may also increase the viscosity of YST to suppress crystal growth at low temperatures. Moreover, Y atoms tend to form more complex structural motifs, which should also contribute to an increase of the energy barrier for crystal nucleation. Further investigations are needed to assess the dynamical changes in YST upon cooling, which would be useful for a fundamental understanding of supercooled liquid PCMs.[56-62]

Before closing, we make a comparison between the new SST and YST alloys with the traditional GST alloys. For the design of SST and YST, Sb_2Te_3 instead of GST was used as the base material to avoid the bonding complexity of Ge atoms in the amorphous phase, namely, the fact that they exhibit both tetrahedral and octahedral coordination,[20-22, 63-67]. It was quantified by orbital-based bonding analysis that the presence of tetrahedral Ge motifs in the amorphous phase was due to the formation of homopolar Ge-Ge bonds during the rapid cooling from the melting phase.[68] Such tetrahedral motifs serve as additional barrier for the crystallization process,[69, 70] and disappear upon aging at room temperature, leading to a pronounced resistance drift.[71, 72] Indeed, it was shown recently that the minimum SET time of Sc alloyed GST devices is ~6 ns,[73] much longer than the ~0.7 ns of SST devices.[32] Alloying elements such as carbon, nitrogen and oxygen are typically incorporated into GST to enhance the amorphous stability.[18] These light alloying atoms typically form very strong but “structurally incompatible” bonds, characterized by short bond lengths below 2.0 Å and non-octahedral bond angles, with Ge, Sb and Te atoms,[74-77] sharply raising the data retention and crystallization temperature. However, these alloying elements also strongly reduce the crystallization dynamics of GST at elevated temperatures, increasing the crystallization time from tens of ns up to several tens of microseconds.[78-80] In comparison, YST retains several bonding similarities, such as comparable bond lengths and high chemical strength, with SST and Sb_2Te_3. This suggests that YST may not sacrifice too much of the switching speed of SST and Sb_2Te_3 (sub-ns and sub-10ns, respectively). We thus anticipate that YST alloys could display high switching speed at elevated temperature combined with enhanced amorphous stability at lower temperatures.

Conclusions

In conclusion, the bonding similarities and differences between yttrium and scandium alloyed Sb_2Te_3 have been thoroughly investigated using a combination of state-of-the-art computational techniques: *ab initio* molecular dynamics simulations, orbital-based chemical bonding analyses, and structural similarity kernels. In a-YST, Y atoms also stabilize local structural motifs with stronger covalent and electrostatic interactions, similar to the situation in a-SST. But the Y- and Sc- centered motifs show clear differences in terms of bond angles, bond lengths and coordination numbers in the two amorphous structures. The smooth overlap of atomic positions analysis quantifies the structural similarity of Y- (or Sc-) centered motifs in amorphous YST (or SST), in comparison with various crystalline yttrium and scandium tellurides. The results reveal

that the bonding contrast around Y and Sc can be understood from the bonding character also found in their crystalline counterparts at high Te concentrations. Despite the isoelectronic valence configuration of Y and Sc, the larger Y atoms form longer bonds with Te atoms, with smaller charge transfer. This gives rise to a lower energy penalty for Te-Te bonds appearing in the Y bonding environment, and thus to a higher coordination number with more Te neighbors and non-octahedral bonds. The more complex Y-Te bonding configuration might render Y-Sb-Te a potential candidate for embedded memory applications which require better room-temperature stability of the amorphous state in combination with a sufficiently high switching speed.

Methods

Density functional theory (DFT) based *ab initio* molecular dynamics (AIMD) simulations were carried out using the second-generation Car-Parrinello scheme,[81] as implemented in the CP2K package.[82] The code employs a mixed scheme of Gaussian-type basis set and plane waves for *ab initio* calculations.[83] The Kohn-Sham orbitals were expanded in Gaussian basis sets with double-zeta and triple-zeta plus polarization quality, whereas the plane waves with a cutoff of 300 Ry were used to calculate the charge density. The Perdew-Burke-Ernzerhof (PBE) functional[84] and Goedecker pseudopotentials[85] were used. The Γ point was used to sample the Brillouin zone of the supercell. AIMD simulations were carried out in the canonical ensemble (NVT) with a stochastic Langevin thermostat. The time step was 2 fs.

The chemical bonding analysis was performed using the crystal orbital Hamilton population (COHP) method,[86] as implemented in the local orbital basis suite towards electronic-structure reconstruction (LOBSTER) code.[87-89] LOBSTER reads the wave functions from plane wave DFT calculations, here using the Vienna Ab initio Simulation Package (VASP),[90] and projects the self-consistent wave functions onto an auxiliary basis of localized, atom-centered orbitals, thereby making complex structural models readily accessible to a chemical interpretation.[91-93] The Löwdin charge analysis[94] was also carried out based on the same projection scheme,[95] as implemented in the LOBSTER code recently. The VASP calculations were done by using the projector augmented-wave (PAW) pseudopotentials and the PBE functional.[84] The cutoff for plane wave expansions was 500 eV. The Brillouin zone was sampled at the Γ point.

Conflicts of interest

The authors declare that they have no conflicts of interest.

Acknowledgments

W.Z. thanks the support of National Natural Science Foundation of China (61774123), 111 Project 2.0 (BP2018008) and the Science and Technology Department of Jiangsu Province (BK20170414). V.L.D. acknowledges a Leverhulme Early Career Fellowship and support from the Isaac Newton Trust. R.M. acknowledges funding from Deutsche Forschungsgemeinschaft (DFG) within SFB 917 (“Nanoswitches”). E.M. is supported at JHU by U.S. Department of Energy (DOE) DOE-BES-DMSE

under grant DE-FG02-19ER46056. The authors acknowledge the computational resources provided by the HPC platform of Xi'an Jiaotong University and JARA-HPC from RWTH Aachen University under project JARA0176. The authors also acknowledge the support by the Materials Studio for Neuro-inspired Computing (mSonic) and the International Joint Laboratory for Micro/Nano Manufacturing and Measurement Technologies of Xi'an Jiaotong University.

References

1. W. Zhang, R. Mazzarello, M. Wuttig and E. Ma, *Nat. Rev. Mater.*, 2019, **4**, 150-168.
2. H.-S. P. Wong and S. Salahuddin, *Nat. Nanotechnol.*, 2015, **10**, 191-194.
3. Y. Yang and R. Huang, *Nat. Electron.*, 2018, **1**, 274-287.
4. Q. Xia and J. J. Yang, *Nat. Mater.*, 2019, **18**, 309-323.
5. C. Y. Wang, C. Wang, F. Meng, P. Wang, S. Wang, S. J. Liang and F. Miao, *Adv. Electron. Mater.*, 2019, **5**, 1901107.
6. F. Zhou, J. Chen, X. Tao, X. Wang and Y. Chai, *Research*, 2019, **2019**, 9490413.
7. Y. van de Burgt, A. Melianas, S. T. Keene, G. Malliaras and A. Salleo, *Nature Electronics*, 2018, **1**, 386-397.
8. A. Chanthbouala, V. Garcia, R. O. Cherifi, K. Bouzehouane, S. Fusil, X. Moya, S. Xavier, H. Yamada, C. Deranlot, N. D. Mathur, M. Bibes, A. Barthelemy and J. Grollier, *Nat. Mater.*, 2012, **11**, 860-864.
9. J. Torrejon, M. Riou, F. A. Araujo, S. Tsunegi, G. Khalsa, D. Querlioz, P. Bortolotti, V. Cros and J. Grollier, *Nature*, 2017, **547**, 428-431.
10. S. W. Fong, C. M. Neumann and H.-S. P. Wong, *IEEE Trans. Electron. Dev.*, 2017, **64**, 4374-4385.
11. J. Hruska, Intel Announces New Optane DC Persistent Memory, https://www.extremetech.com/extreme/270270-intel-announces-new-optane-dc-persistent-memory.
12. M. Wuttig and N. Yamada, *Nat. Mater.*, 2007, **6**, 824-832.
13. M. Salinga, B. Kersting, I. Ronneberger, V. P. Jonnalagadda, X. T. Vu, M. L. Gallo, I. Giannopoulos, O. Cojocaru-Mirédin, R. Mazzarello and A. Sebastian, *Nat. Mater.*, 2018, **17**, 681-685.
14. W. Zhang and E. Ma, *Nat. Mater.*, 2018, **17**, 654-655.
15. W. Zhang, R. Mazzarello and E. Ma, *MRS Bulletin*, 2019, **44**, 686-690.
16. A. Sebastian, M. Le Gallo, G. W. Burr, S. Kim, M. BrightSky and E. Eleftheriou, *J. Appl. Phys.*, 2018, **124**, 111101.
17. K. Ding, J. Wang, Y. Zhou, H. Tian, L. Lu, R. Mazzarello, C. Jia, W. Zhang, F. Rao and E. Ma, *Science*, 2019, **366**, 210-215.
18. H.-S. P. Wong, S. Raoux, S. B. Kim, J. Liang, J. P. Reifenberg, B. Rajendran, M. Asheghi and K. E. Goodson, *Proc. IEEE*, 2010, **98**, 2201.
19. S. Kohara, K. Kato, S. Kimura, H. Tanaka, T. Usuki, K. Suzuya, H. Tanaka, Y. Moritomo, T. Matsunaga, N. Yamada, Y. Tanaka, H. Suematsu and M. Takata, *Appl. Phys. Lett.*, 2006, **89**, 201910.
20. S. Caravati, M. Bernasconi, T. D. Kühne, M. Krack and M. Parrinello, *Appl. Phys. Lett.*, 2007, **91**, 171906.
21. J. Akola and R. Jones, *Phys. Rev. B,* 2007, **76**, 235201.
22. M. Xu, Y. Cheng, H. Sheng and E. Ma, *Phys. Rev. Lett.*, 2009, **103**, 195502.
23. J. Hegedüs and S. R. Elliott, *Nat. Mater.*, 2008, **7**, 399-405.
24. J. Kalikka, J. Akola, J. Larrucea and R. O. Jones, *Phys. Rev. B*, 2012, **86**, 144113.
25. J. Kalikka, J. Akola and R. O. Jones, *Phys. Rev. B*, 2014, **90**, 184109.
26. J. Kalikka, J. Akola and R. O. Jones, *Phys. Rev. B*, 2016, **94**, 134105.
27. I. Ronneberger, W. Zhang, H. Eshet and R. Mazzarello, *Adv. Funct. Mater.*, 2015, **25**, 6407-6413.

28. I. Ronneberger, W. Zhang and R. Mazzarello, *MRS Comm.*, 2018, **8**, 1018-1023.
29. D. Loke, T. H. Lee, W. J. Wang, L. P. Shi, R. Zhao, Y. C. Yeo, T. C. Chong and S. R. Elliott, *Science*, 2012, **336**, 1566-1569.
30. D. K. Loke, J. M. Skelton, T. H. Lee, R. Zhao, C.-T. Chong and S. R. Elliott, *ACS Appl. Mater. Interfaces*, 2018, **10**, 41855-41860.
31. J. Orava and A. L. Greer, *Acta Mater.*, 2017, **139**, 226-235.
32. F. Rao, K. Ding, Y. Zhou, Y. Zheng, M. Xia, S. Lv, Z. Song, S. Feng, I. Ronneberger, R. Mazzarello, W. Zhang and E. Ma, *Science*, 2017, **358**, 1423-1427.
33. S. Hu, B. Liu, Z. Li, J. Zhou and Z. Sun, *Comput. Mater. Sci.*, 2019, **165**, 51-58.
34. C. Qiao, Y. R. Guo, S. Y. Wang, M. Xu, X. Miao, C. Z. Wang and K. M. Ho, *Appl. Phys. Lett.*, 2019, **114**, 071901.
35. G. M. Zewdie, Y. Zhou, L. Sun, F. Rao, V. L. Deringer, R. Mazzarello and W. Zhang, *Chem. Mater.*, 2019, **31**, 4008−4015.
36. Z. Li, C. Si, J. Zhou, H. Xu and Z. Sun, *ACS Appl. Mater. Interfaces*, 2016, **8**, 26126-26134.
37. Z. Li, N. Miao, J. Zhou, H. Xu and Z. Sun, *J. Appl. Phys.*, 2017, **122**, 195107.
38. T. Li, L. Wu, Y. Wang, G. Liu, T. Guo, S. Song and Z. Song, *Mater. Lett.*, 2019, **247**, 60-62.
39. X. Chen, Y. Zheng, M. Zhu, K. Ren, Y. Wang, T. Li, G. Liu, T. Guo, L. Wu, X. Liu, Y. Cheng and Z. Song, *Sci. Rep.*, 2018, **8**, 6839.
40. S. Caravati, M. Bernasconi and M. Parrinello, *Phys. Rev. B*, 2010, **81**, 014201.
41. W. Zhang, I. Ronneberger, Y. Li and R. Mazzarello, *Chem. Month.*, 2014, **145**, 97-101.
42. Y. Guo, F. Dong, C. Qiao, J. Wang, S. Wang, M. Xu, Y. Zheng, R. Zhang, L. Chen, C. Wang and K. Ho, *Phys. Chem. Chem. Phys.*, 2018, **20**, 11768-11775.
43. A. P. Bartók, R. Kondor and G. Csányi, *Phys. Rev. B*, 2013, **87**, 184115.
44. S. De, A. P. Bartók, G. Csányi and M. Ceriotti, *Phys. Chem. Chem. Phys.*, 2016, **18**, 13754-13769.
45. V. L. Deringer, M. A. Caro, R. Jana, A. Aarva, S. R. Elliott, T. Laurila, G. Csányi and L. Pastewka, *Chem. Mater.*, 2018, **30**, 7438-7445.
46. N. Bernstein, B. Bhattarai, G. Csányi, D. A. Drabold, S. R. Elliott and V. L. Deringer, *Angew. Chem. Int. Ed.*, 2019, **58**, 7057-7061.
47. E. A. Engel, A. Anelli, M. Ceriotti, C. J. Pickard and R. J. Needs, *Nat. Comm.*, 2018, **9**, 2173.
48. J. Mavračić, F. C. Mocanu, V. L. Deringer, G. Csányi and S. R. Elliott, *J. Phys. Chem. Lett.*, 2018, **9**, 2985-2990.
49. L. Himanen, M. O. J. Jäger, E. V. Morooka, F. Federici Canova, Y. S. Ranawat, D. Z. Gao, P. Rinke and A. S. Foster, *Comp. Phys. Comm.*, 2020, **247**, 106949.
50. L. H. Brixner, *J. Inorg. Nucl. Chem.*, 1960, **15**, 199-201.
51. J. P. Dismukes and J. G. White, *Inorg. Chem.*, 1965, **4**, 970-973.
52. J. F. Cannon and H. T. Hall, *Inorg. Chem.*, 1970, **9**, 1639-1643.
53. F. J. Pardo M.P., *Bulletin de la Societe Chimique de France*, 1967, **114**, 3658-3664.
54. A. A. Men'kov, Komissarova, L. N., Simanov, Y. P., *Doklady Akademii Nauk SSSR*, 1961, **141**, 364-367.
55. B. Chen, Y. Chen, K. Ding, K. Li, F. Jiao, L. Wang, X. Zeng, J. Wang, X. Shen, W. Zhang, F. Rao and E. Ma, *Chem. Mater.*, 2019, **31**, 8794-8800.
56. J. Orava, A. L. Greer, B. Gholipour, D. W. Hewak and C. E. Smith, *Appl. Phys. Lett.*, 2012, **101**, 091906.
57. J. Orava, H. Weber, I. Kaban and A. L. Greer, *J. Chem. Phys.*, 2016, **144**, 194503.
58. J. Orava, D. W. Hewak and A. L. Greer, *Adv. Funct. Mater.*, 2015, **25**, 4851-4858.
59. P. Zalden, F. Quirin, M. Schumacher, J. Siegel, S. Wei, A. Koc, M. Nicoul, M. Trigo, P. Andreasson, H. Enquist, M. Shu, T. Pardini, M. Chollet, D. Zhu, H. Lemke, I. Ronneberger, J. Larsson, A. M.

Lindenberg, H. E. Fischer, S. Hau-Riege, D. A. Reis, R. Mazzarello, M. Wuttig and K. Sokolowski-Tinten, *Science*, 2019, **364**, 1062–1067.
60. F. Rao, W. Zhang and E. Ma, *Science*, 2019, **364**, 1032-1033.
61. J. Pries, S. Wei, M. Wuttig and P. Lucas, *Adv. Mater.*, 2019, **31**, 1900784.
62. S. Wei, P. Lucas and C. A. Angell, *MRS Bulletin*, 2019, **44**, 691-698.
63. A. V. Kolobov, P. Fons, A. I. Frenkel, A. L. Ankudinov, J. Tominaga and T. Uruga, *Nat. Mater.*, 2004, **3**, 703-708.
64. J. Akola, R. Jones, S. Kohara, S. Kimura, K. Kobayashi, M. Takata, T. Matsunaga, R. Kojima and N. Yamada, *Phys. Rev. B*, 2009, **80**, 020201.
65. X. Q. Liu, X. B. Li, L. Zhang, Y. Q. Cheng, Z. G. Yan, M. Xu, X. D. Han, S. B. Zhang, Z. Zhang and E. Ma, *Phys. Rev. Lett.*, 2011, **106**, 025501.
66. M. Krbal, A. V. Kolobov, P. Fons, K. V. Mitrofanov, Y. Tamenori, J. Hegedüs, S. R. Elliott and J. Tominaga, *Appl. Phys. Lett.*, 2013, **102**, 111904.
67. C. Qiao, Y. R. Guo, F. Dong, J. J. Wang, H. Shen, S. Y. Wang, M. Xu, X. S. Miao, Y. X. Zheng, R. J. Zhang, L. Y. Chen, C. Z. Wang and K. M. Ho, *J. Mater. Chem. C*, 2018, **6**, 5001-5011.
68. V. L. Deringer, W. Zhang, M. Lumeij, S. Maintz, M. Wuttig, R. Mazzarello and R. Dronskowski, *Angew. Chem. Int. Ed.* , 2014, **53**, 10817-10820.
69. T. H. Lee and S. R. Elliott, *Phys. Rev. Lett.*, 2011, **107**, 145702.
70. T. H. Lee and S. R. Elliott, *Adv. Mater.*, 2017, **29**, 1700814.
71. K. V. Mitrofanov, A. V. Kolobov, P. Fons, X. Wang, J. Tominaga, Y. Tamenori, T. Uruga, N. Ciocchini and D. Ielmini, *J. Appl. Phys.*, 2014, **115**, 173501.
72. J.-Y. Raty, W. Zhang, J. Luckas, C. Chen, C. Bichara, R. Mazzarello and M. Wuttig, *Nat. Commun.*, 2015, **6**, 7467.
73. Y. Wang, Y. Zheng, G. Liu, T. Li, T. Guo, Y. Cheng, S. Lv, S. Song, K. Ren and Z. Song, *Appl. Phys. Lett.*, 2018, **112**, 133104.
74. S. Caravati, D. Colleoni, R. Mazzarello, T. D. Kuhne, M. Krack, M. Bernasconi and M. Parrinello, *J. Phys. Condens. Matter*, 2011, **23**, 265801.
75. E. Cho, S. Han, D. Kim, H. Horii and H.-S. Nam, *J. Appl. Phys.*, 2011, **109**, 043705.
76. T. H. Lee, D. Loke and S. R. Elliott, *Adv. Mater.*, 2015, **27**, 5477-5483.
77. L. Zhu, Z. Li, J. Zhou, N. Miao and Z. Sun, *J. Mater. Chem. C*, 2017, **5**, 3592-3599.
78. R. M. Shelby and S. Raoux, *J. Appl. Phys.*, 2009, **105**, 104902.
79. T. Li, J. Shen, L. Wu, Z. Song, S. Lv, D. Cai, S. Zhang, T. Guo, S. Song and M. Zhu, *J. Phys. Chem. C,* 2019, **123**, 13377-13384.
80. X. Li, H. Chen, C. Xie, D. Cai, S. Song, Y. Chen, Y. Lei, M. Zhu and Z. Song, *Phys. Status Solidi RRL*, 2019, **13**, 1800558.
81. T. Kühne, M. Krack, F. Mohamed and M. Parrinello, *Phys. Rev. Lett.*, 2007, **98**, 066401.
82. J. Hutter, M. Iannuzzi, F. Schiffmann and J. VandeVondele, *WIREs Comput. Mol. Sci.* , 2014, **4**, 15-25.
83. J. VandeVondele, M. Krack, F. Mohamed, M. Parrinello, T. Chassaing and J. Hutter, *Comput. Phys. Comm.*, 2005, **167**, 103-128.
84. J. P. Perdew, K. Burke and M. Ernzerhof, *Phys. Rev. Lett.*, 1996, **77**, 3865-3868.
85. S. Goedecker, M. Teter and J. Hutter, *Phys. Rev. B*, 1996, **54**, 1703.
86. R. Dronskowski and P. E. Blöchl, *J. Phys. Chem.*, 1993, **97**, 8617-8624
87. V. L. Deringer, A. L. Tchougreeff and R. Dronskowski, *J. Phys. Chem. A*, 2011, **115**, 5461-5466.
88. S. Maintz, V. L. Deringer, A. L. Tchougréeff and R. Dronskowski, *J. Comput. Chem.*, 2013, **34**, 2557-2567.
89. S. Maintz, V. L. Deringer, A. L. Tchougreeff and R. Dronskowski, *J. Comput. Chem.*, 2016, **37**, 1030-1035.

90. G. Kresse and J. Hafner, *Phys. Rev. B*, 1993, **47**, 558-561.
91. V. L. Deringer, R. Dronskowski and M. Wuttig, *Adv. Funct. Mater.*, 2015, **25**, 6343-6359.
92. V. L. Deringer, W. Zhang, P. Rausch, R. Mazzarello, M. Wuttig and R. Dronskowski, *J. Mater. Chem. C*, 2015, **3**, 9519-9523.
93. Y. Chen, L. Sun, Y. Zhou, G. M. Zewdie, V. L. Deringer, R. Mazzarello and W. Zhang, *J. Mater. Chem. C*, 2020, **8**, 71-77.
94. P. O. Löwdin, *J. Chem. Phys.*, 1950, **18**, 365−375.
95. C. Ertural, S. Steinberg and R. Dronskowski, *RSC Adv.*, 2019, **9**, 29821-29830.

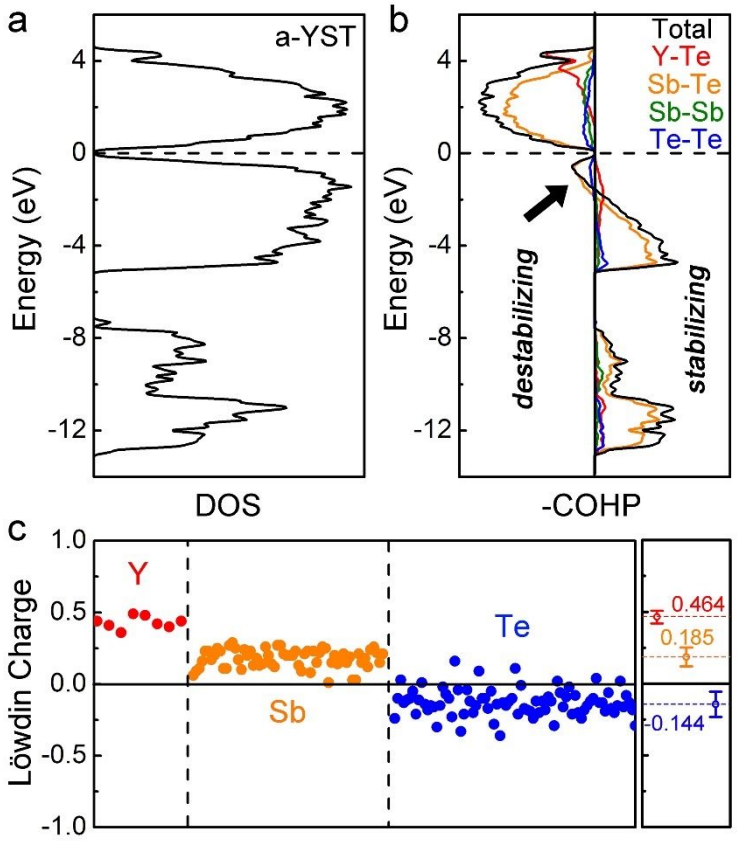

Figure 1. (a) The density of states (DOS), (b) the COHP analysis and (c) the Löwdin charge analysis of a-YST. Amorphous YST shows a narrow band gap. Projected COHP curves for Y-Te, Sb-Te, Sb-Sb and Te-Te contacts are shown, while no Y-Y and Y-Sb contacts are found in the amorphous models. Contributions are collected from all atomic interactions up to 3.4 Å for COHP analysis. The average values of computed Löwdin charges are 0.464, 0.185 and -0.144 |e| for Y, Sb and Te atoms, respectively.

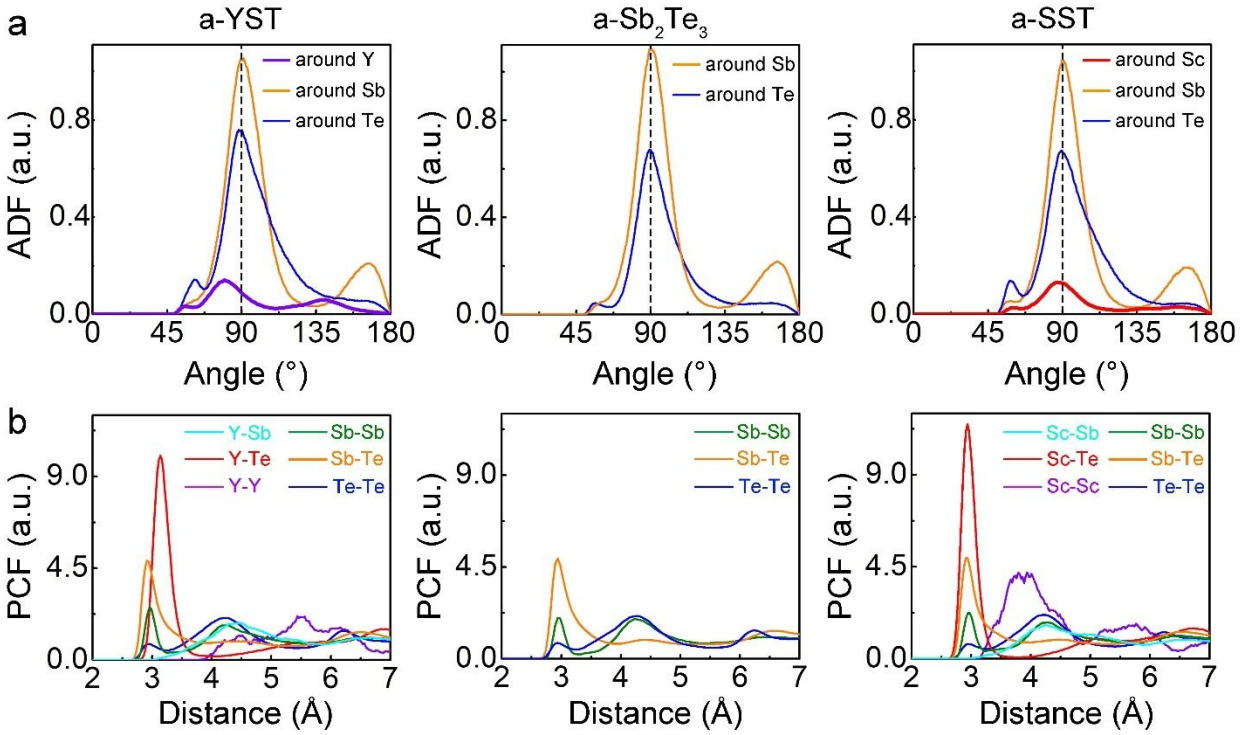

Figure 2. (a) The angular distribution functions (ADFs) and (b) the partial pair correlation functions (PCFs) of amorphous YST, Sb_2Te_3 and SST models. All the ADFs and PCFs data were collected from five independent amorphous models over 10 ps at 300 K.

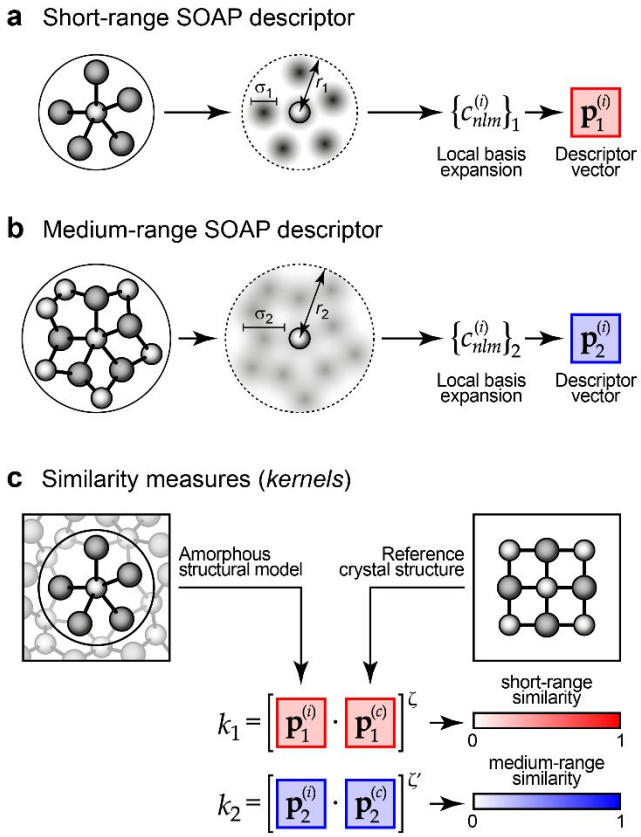

Figure 3. The principle of smooth overlap of atomic positions (SOAP) based structural analyses. (a) Construction of a SOAP descriptor vector based on the short-range structural environment of a given atom, up to a given cut-off radius r_1. The atomic neighbor density is described by Gaussian functions of smoothness σ_1, and expanded into atom-centered basis functions with coefficients c. Details of the formalism are given in Ref. [43]. (b) Same but now for the analysis of the medium-range structure: the analysis extends further ($r_2 > r_1$) and is based on a smoother neighbor density ($\sigma_2 > \sigma_1$); cf. Ref. [46]. (c) Construction of quantitative similarity measures (SOAP kernels) for short- and medium-range similarity, which form the basis of the analyses for YST and SST in the present work.

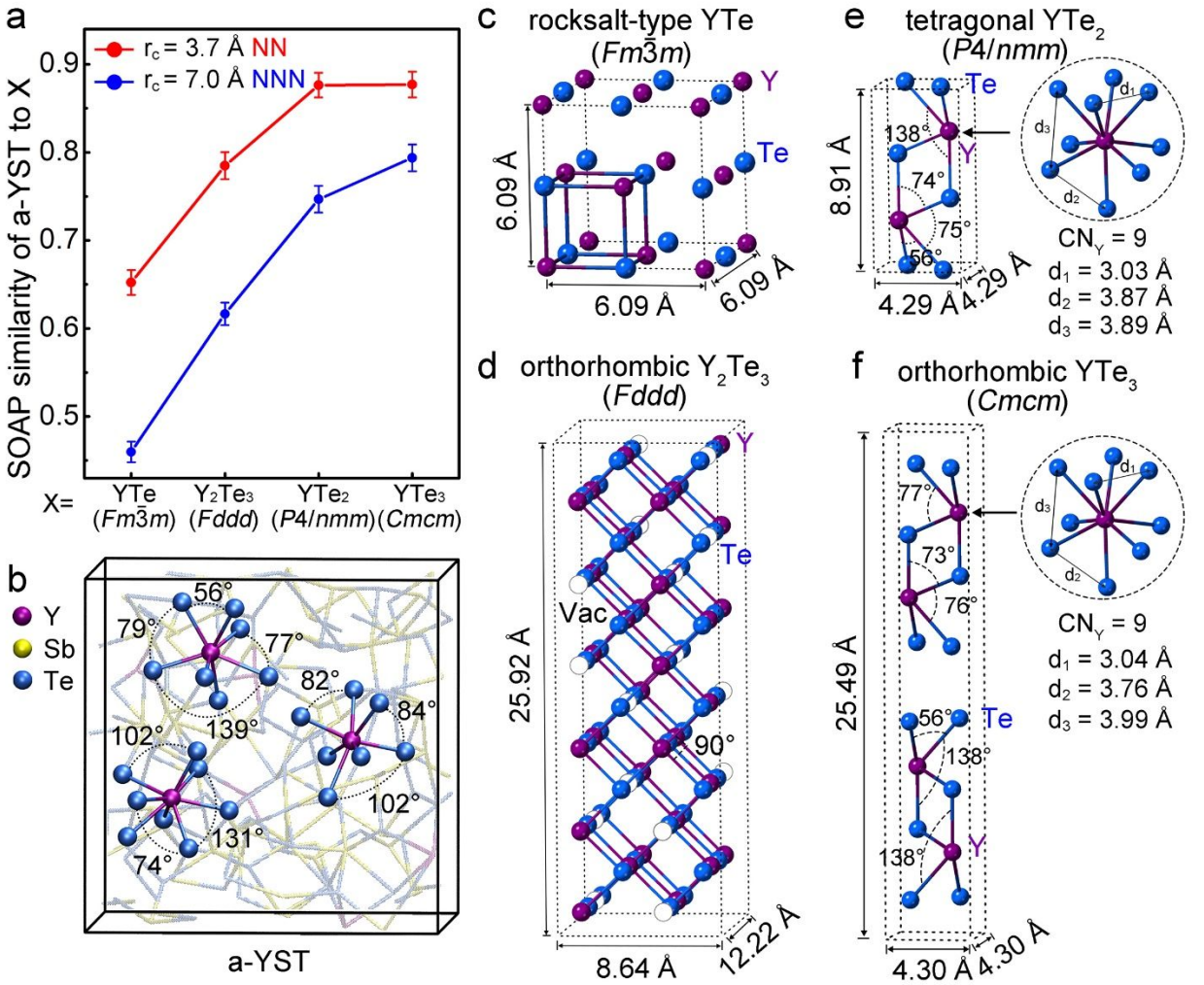

Figure 4. (a) The SOAP description of Y-centered motifs in a-YST in comparison with four yttrium telluride crystal structures. Lines connecting data points are guides to the eye. We use r_c = 3.7 Å and r_c = 7.0 Å for nearest neighbor (NN) and next-nearest neighbor (NNN) analysis, respectively. An average is made over all Y-centered motifs in five independent a-YST models. (b) A snapshot of a-YST, with a couple of Y-centered motifs highlighted. (c) Rocksalt YTe.[50] The Y-Te bond length is 3.05 Å. (d) Orthorhombic Y_2Te_3.[51] 1/3 sites of the cation-like sublattice are atomic vacancies that are arranged in an ordered fashion. The Y-Te bond length is 3.07 Å. (e)-(f) Tetragonal YTe_2 [52] and orthorhombic YTe_3.[53] The Y-Te bond length ranges from 3.15 Å to 3.25 Å. All the supercell dimensional parameters and bond lengths of Y-Te crystals are experimental values.[50-53]

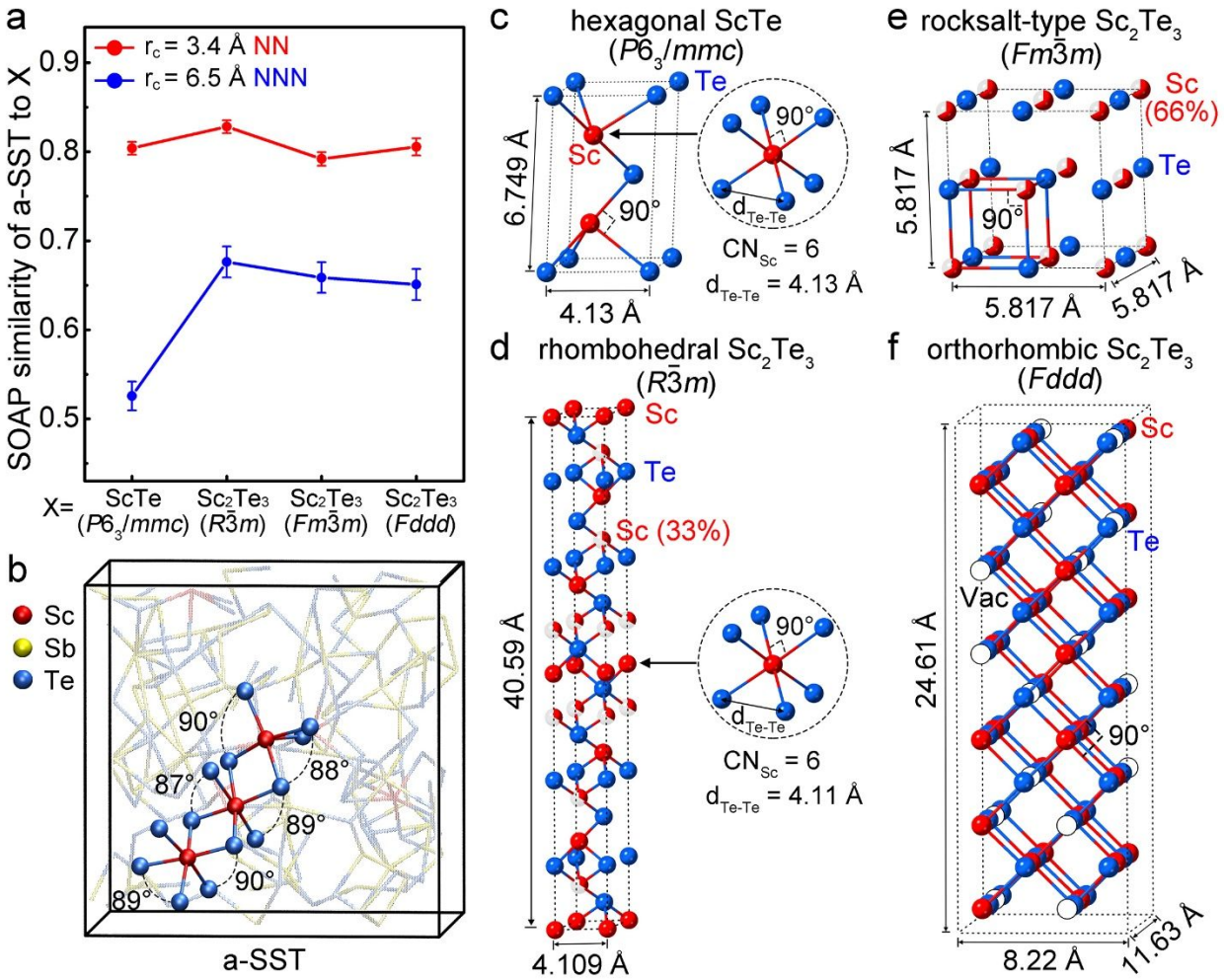

Figure 5. (a) The SOAP description of Sc-centered motifs in a-SST with respect to four scandium telluride crystal structures. We use r_c = 3.4 Å and r_c = 6.5 Å for nearest neighbor (NN) and next-nearest neighbor (NNN) similarity analysis, respectively. (b) A snapshot of a-SST, with a couple of Sc-centered motifs highlighted. (c) Hexagonal ScTe.[54] The Sc-Te bond length is 2.92 Å. (d) Rhombohedral Sc_2Te_3. The Sc-Te bond length is 2.95 Å. 1/3 sites in every second Sc layer are randomly distributed atomic vacancies. (e) Rocksalt-type Sc_2Te_3 with 1/3 sites of the cation-like sublattice being occupied by randomly distributed atomic vacancies. The Sc-Te bond length is 2.91 Å. (f) Orthorhombic Sc_2Te_3. 1/3 sites of the cation-like sublattice are atomic vacancies that are arranged in an ordered fashion. The Sc-Te bond length is 2.91 Å. All the Sc atoms form a perfect octahedral configuration in the four crystal structures. All the lattice parameters and bond lengths of Sc-Te crystals are experimental values.[35, 54]

Table 1. The nearest neighbor (NN) and next-nearest neighbor (NNN) SOAP-kernel-based similarity k_{ij} of four crystalline yttrium tellurides, when compared to one another (*i, j* = rocksalt YTe, orthorhombic Y_2Te_3, tetrahedral YTe_2 and orthorhombic YTe_3).

Length scale		**NN, r_c = 3.7 Å**				**NNN, r_c = 7.0 Å**			
		j =				*j* =			
	k_{ij}	Rocksalt YTe	Orthro-Y_2Te_3	Tetra-YTe_2	Orthor-YTe_3	Rocksalt YTe	Orthro-Y_2Te_3	Tetra-YTe_2	Orthor-YTe_3
i =	Rocksalt YTe	1.000	0.961	0.774	0.762	1.000	0.953	0.782	0.706
	Orthro-Y_2Te_3		1.000	0.839	0.829		1.000	0.889	0.847
	Tetra-YTe_2			1.000	0.999			1.000	0.982
	Orthor-YTe_3				1.000				1.000

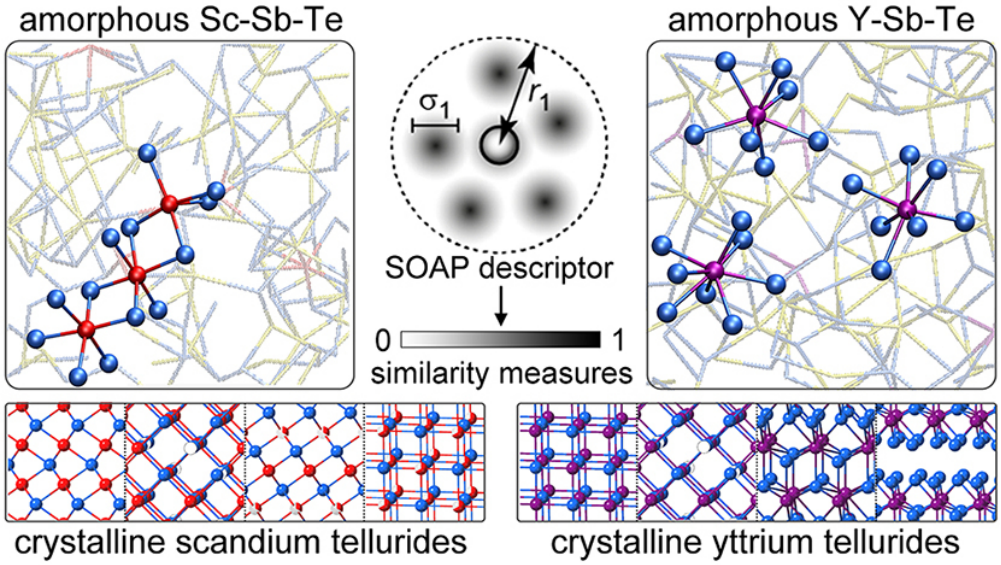
amorphous Sc-Sb-Te
amorphous Y-Sb-Te
σ1
r1
SOAP descriptor
0
1
similarity measures
crystalline scandium tellurides
crystalline yttrium tellurides